JOURNAL OF MATERIALS SCIENCE 23 (1988) 3006–3014

Sliding contact fracture on glass and silicon

H. J. LEU, R. O. SCATTERGOOD
Department of Materials Engineering, North Carolina State University, Raleigh, North Carolina 27695-7907, USA

Surface crack geometry produced during sliding contact on amorphous glass specimens and silicon single-crystal specimens was investigted. The experiments were performed by sliding a spherical indentor on a surface with increasing normal load in ambient air and oil environments. The results show that the cracks formed on the contact surface due to sliding motion are governed by the stress field generated. Cracks tend to follow the maximum principal tensile stress trajectories in amorphous glass specimens, but the cracks generated on silicon were strongly influenced by the planes of easy cleavage on the contact surface. The normal load P, friction coefficient of contact and crystallographic cleavage plane directions were found to have a large influence on the surface crack patterns. A general relation, $W \propto P^{1/3}$, was obtained for the measurement of crack widths W in all testing conditions. Crack-morphologies were related to material removal. Studies showed that the latter is often due to chip formation which occurs between very closely spaced cracks.

1. Introduction

Static or sliding contact between surfaces is important for the wear of brittle materials. Most of the previous studies were conducted by the static indentation of a spherical indentor. Much work has been done on the characterization of the static phenomena, but relatively little work concerning the indentation damage with sliding motion across the contact surface has been reported. The study of abrasion and fracture due to sliding contact is applicable and important for tribological applications, for example, wear in ceramic bearing and valve guides, or wear-resistant coatings.

The static Hertzian fracture test, in which a hard spherical indentor is loaded on to a flat brittle substance without sliding motion, produces a well-defined circular ring crack pattern on the surface. With further increases in the load, the ring cracks develop into multiple ring cracks and cone cracks, which extend beneath the contact surface of the specimen.

The contact geometry beneath a smooth spherical indentor loaded on to a flat plate was calculated by Hertz [1] for a brittle, isotropic material. The ideal Hertzian elastic contact is well defined up to the initial fracture in a perfectly elastic–brittle material. The first elastic stress field solution for static contact in an isotropic material was produced by Von Huber [2]. Under static conditions, the applied load is distributed as a hemisphere of compressive stresses inside the contact circle [3]. The maximum tensile stress on the specimen surface occurs at the contact edge and is radially directed. To discuss the probable crack paths in a single-crystal specimen, Lawn [4] discussed in detail the distribution of the three principal stresses σ_{11}, σ_{22}, σ_{33} and their directions by means of stress trajectories. The contours of the principal stresses were also provided.

Sliding contact geometry is shown schematically in Fig. 1a. The first sliding contact tests, and the associated crack patterns, were investigated by Preston [5] on flat glass plates and by Seal [6] on diamond. The complete quasi-static stress field around a sliding contact was solved analytically by Hamilton and Goodman [7].

In Preston's early investigations, some preliminary observations on hard brittle substances were recorded where the crack patterns were produced by stationary rolling and sliding spheres, or by glazier diamonds and wheels. Later, Lawn 83] took the indentor and the specimen to be purely elastic and elastic–brittle solids, respectively, and assumed a uniform coefficient of friction over the contact area. He found that the sliding has a large influence on the quasi-static stress field in the loaded specimen and this, in turn, affects the ultimate geometry of the cracks. The precise shape of the cracks thus formed is a function of Poisson's ratio of the specimen and the coefficient of friction [3]. The cracks on the contacting surface can be switched from complete ring cracks to open partial ring cracks with the increase of the coefficient of interfacial friction, f.

Griffith's pioneer paper [8] identified the important criteria for the initiation and propagation of cracks. For indentation tests, the initiation begins from "flaws", either pre-existing or induced by the indentation itself. An essential step in developing fracture mechanics requires the analysis of crack geometry. For an ideally brittle isotropic solid, starting from a critical flaw, the ultimate path of the crack corresponds to the maximization of the mechanical energy release rate. Basically, the crack tends at any point to propagate along trajectories of lesser principal stress in the prior fields, thereby maintaining near orthogonality to the major component of tension, i.e. along the maximum tensile principal stress contours.

0022–2461/88 $03.00 + .12

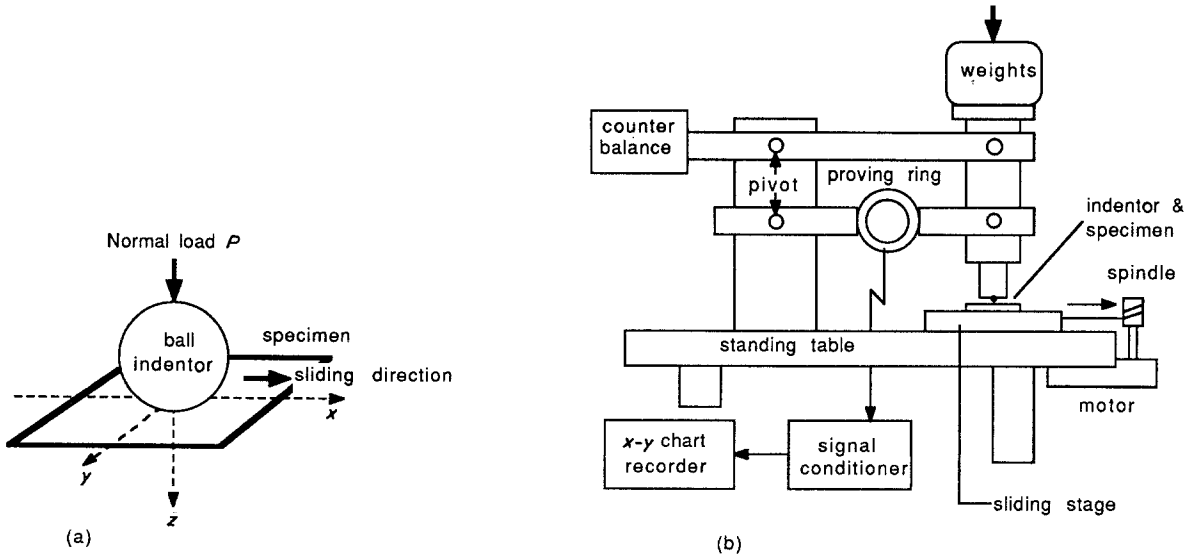

Figure 1 Schematic drawing of (a) sliding contact geometry, (b) test apparatus.

The Hertzian ring crack morphology in single crystals is dependent on the crystal orientation, especially at certain favourable loads, where the surface crack traces reflect the symmetry of the crystal structure [9]. From the analysis of the cleavage traces in silicon, the initial stage of crack growth near the crystal surface appears to proceed along favourably oriented {1 1 1} cleavage planes [9]. However, on examination of cracks below the crystal surface, it is always found that the path tends to deviate away from {1 1 1} planes toward the Hertzian cone, and thus to follow the maximum principal stress trajectories as it propagates into the interior.

In the work reported here, systematic observations were made of sliding contact fracture patterns on glass and silicon single crystals. The effect of friction and crystallography can be evaluated separately from each other using these samples.

2. Experimental procedures

The basic testing procedure involved making crack patterns by sliding (non-rolling) spherical indentors on glass and on silicon single-crystal plates in various orientations under different conditions. Tests were performed using different size chrome steel balls and tungsten carbide balls. Transparent commercial soda–lime window glass was used. As-received glass was etched 3 h in 5% HF solution as the standard pre-etching procedure. Three other surface etching procedures, no etching, 15 min etching, and 45 min etching in 5% HF solution, were also used to compare surface etching effects.

Semiconductor grade silicon single-crystal ingots were kindly supplied by R. Frederick (Monsanto Co., St Peter, Missouri). The cut silicon plates were ground successively on 100–240–400–600 grit silicon carbide grinding papers, then polished with 6–1–$\frac{1}{4}$ μm diamond pastes. The specific crystallographic plane and direction on which the sliding tracks were made were within 3° of the specified orientations according to back-reflection Laue patterns. Apart from cutting and find polishing, no additional surface treatment was used for the silicon crystals.

Sliding contact tests were performed with a modified pin-on-disc wear machine, shown in Fig. 1b. Friction force was recorded using a proving ring with strain gauges. The output was recorded on a chart recorder and the friction coefficient for a sliding test is defined as $f = P_T/P$ where P_T is the average tangential force obtained from the chart. Normal force, P, was fixed by dead-weight loading. The upper limit for P was 200 to 250 N, which was fixed by constraints due to the apparatus. Ball indentors were changed after every ten sliding tests to minimize surface damage and geometry change of the indentor. A standard pulling speed of 56 mm min^{-1} was used unless noted otherwise. Tests were made in ambient air and under STP oil. The latter was used to change the frictional properties because it is an excellent low-friction polymer-based lubricant. All tests were done at room temperature.

The sliding contact tracks were etched with Dash's solution [10] for both glass and silicon for 1 to 2 min at room temperature to reveal the surface crack morphologies. After etching, the surface was lightly repolished with 1 μm diamond compound to remove the initial surface polishing scratches revealed by etching.

3. Results

3.1. Surface crack patterns

Typical sliding contact crack patterns for glass are shown in Figs 2 to 5. The cracks were generated in oil and in air using tungsten carbide or chrome steel balls in the size range 1 to 3 mm. The ball type or size did not influence the results except that to obtain equivalent crack patterns, a larger normal load is needed with larger ball sizes. The friction coefficients, f, fell in the range $f \approx 0.1$ to 0.3. Tests in oil tended to produce values of $f \approx 0.1$ or less while those in air produced values of $f \approx 0.3$. However, there was some variability in the friction values. In about one-third of the tests, the values of f in air were in the region $f \approx 0.1$. Furthermore, some of the tests in oil produced high values of f. Nevertheless, the principal features in the crack patterns could be correlated with f and P, regardless of

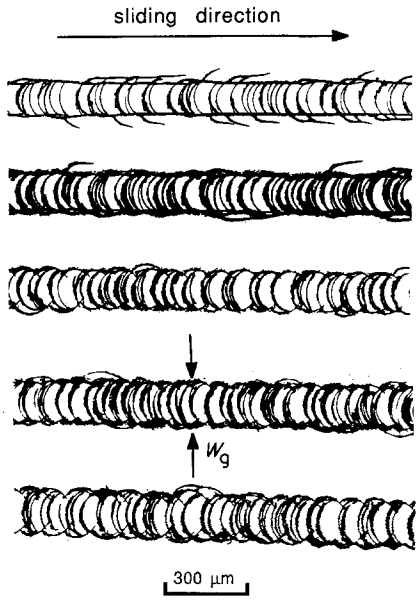

Figure 2 Surface crack patterns on glass produced in air with 1.0 mm WC ball showing envelope cracks and partial ring cracks, $f \approx 0.1$, P = 22, 23, 33, 44, 55, 66 N top to bottom, respectively.

the test environment. The only recognizable effect of the environment for the tests reported here was in controlling the value of the friction coefficient.

Fig. 2 shows typical sliding contact crack patterns for a test sequence corresponding to low values of friction in air in the range $f \approx 0.1$. The patterns appear as sequences of partial ring cracks along the sliding track. As P increases, the density of cracks increases and at the higher loads there is minor chipping damage. As will be mentioned later, there are actually two crack systems formed. Partial ring cracks occur within the track and a system of envelope cracks occurs parallel to the sliding direction at the outer edges of the track.

Fig. 3 shows a typical series of crack patterns cor-

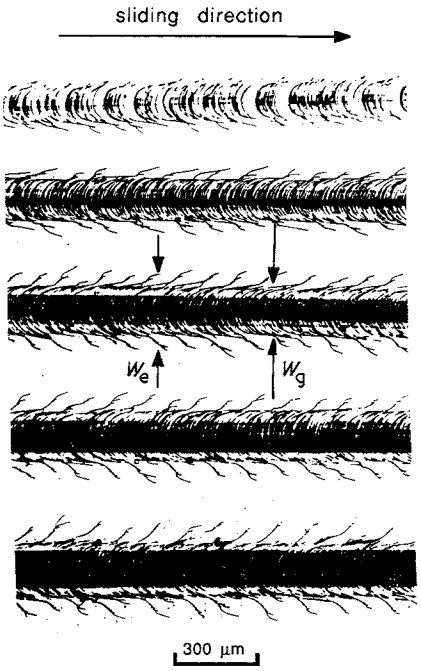

Figure 3 Surface crack patterns on glass produced in air with 1.0 mm WC ball showing extended cracks, $f \approx 0.3$, P = 22, 33, 44, 55, 66 N top of bottom, respectively.

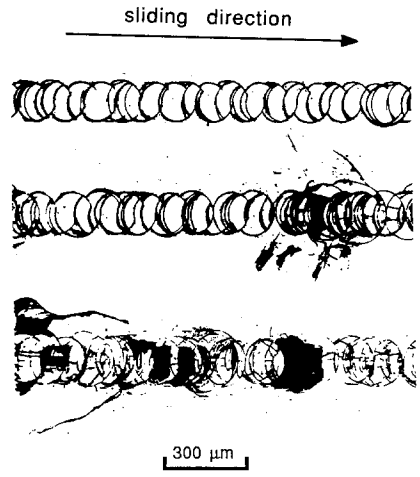

Figure 4 Surface crack patterns on glass produced in oil with 1.0 mm WC ball showing envelope cracks and partial ring cracks, $f \approx 0.05$ to 0.1, P = 44, 55, 66 N top to bottom, respectively.

responding to high values of friction in the range $f \approx 0.3$. In this case, a different crack morphology occurs. Partial ring cracks still occur within the sliding track and their density increases significantly with load. However, the partial ring cracks are more open than in the lower friction tests. Furthermore, a distinct envelope of cracks bounding the track does not form, although there is a tendency for the partial ring cracks to deflect somewhat along the edges of the track. At higher loads the partial ring cracks branch outward away from the track forming a quasi-periodic system of "extended" cracks. There is also extensive damage within the track in the form of wear scars and grooves, visible as dark regions within the track. The latter no doubt contribute to the high friction conditions reflected in the higher f values.

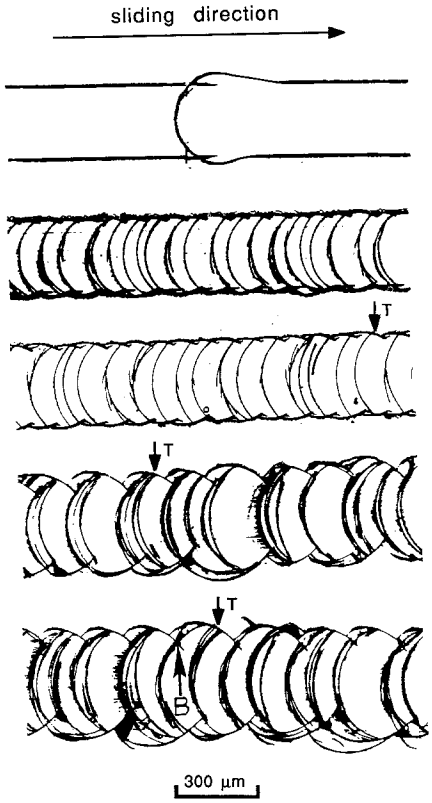

Figure 5 Surface crack patterns on glass produced in oil with 3.15 mm steel ball showing envelope cracks and partial ring cracks, $f \approx 0.1$, P = 110, 133, 15, 244, 288 N top to bottom, respectively.

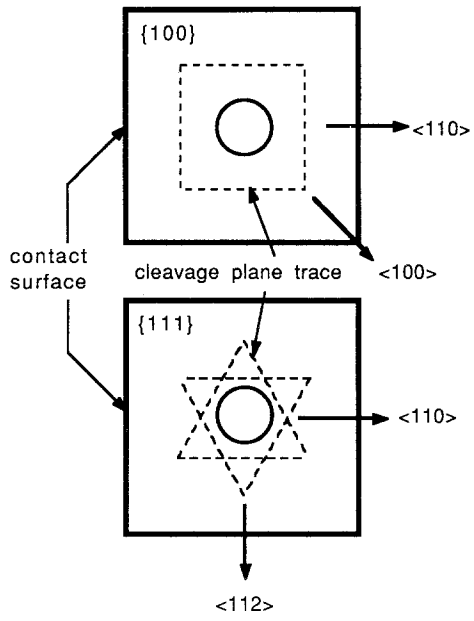

Figure 6 Schematic drawing of sliding systems on silicon. Dash lines show {1 1 1} cleavage plane intersections.

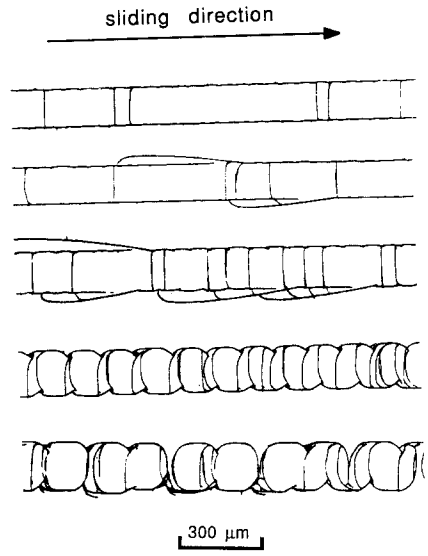

Figure 7 Surface crack patterns on silicon produced in air with 1.55 mm steel ball showing envelope cracks and partial ring cracks for {0 0 1} ⟨1 1 0⟩ sliding system. $f \approx 0.1$, P = 22, 33, 44, 55, 66 N top to bottom, respectively.

Fig. 4 shows a series of crack patterns obtained in oil, which correspond to the lowest values of friction obtainable in the range $f \approx 0.05$ to 0.1. These are similar to the patterns in Fig. 2, except that almost fully closed ring cracks can sometimes be generated at the higher values of P. Extensive chipping damage also occurs in Fig. 4 at the higher loads. Chipping damage of this type for a 1.0 mm ball size at low values of f was a common feature for the tests in both glass and silicon single crystal surfaces.

Fig. 5 shows a series of cracks patterns for conditions similar to those in Fig. 4, but with a 3.15 mm steel slider ball. Increasing the ball size did not significantly affect the crack patterns except that the patterns become wider relative to smaller ball sizes, and higher loads are needed to obtain equivalent crack morphologies. As will be noted further in the discussion, the load P must be increased by about an order of magnitude to obtain the same mean Hertzian contact pressure for a 3.15 mm (Fig. 5) compared to a 1.0 mm (Fig. 4) ball. Fig. 5 (top frame) shows an effect that often occurs at low loads, especially with the larger ball size. The crack pattern is comprised of a pair of straight, parallel envelope cracks, which are drawn along the edges of the sliding track, sometimes interrupted by the formation of a single partial ring crack as seen in the figure (top frame).

Two crack width parameters can be defined as indicated in Figs 2 and 3. The general crack width, W_g, is the width of the main body of partial ring cracks in the sliding track, often bounded by envelope cracks. The extended crack width, W_e, is the maximum width of the extended cracks that branch outward from the main body of cracks. A well-defined, quasi-periodic system of extended cracks is observed only at higher f values.

The general features of the sliding-contact crack patterns generated on silicon single crystals are similar to those occurring on glass, but there is a significant effect of the crystal orientation. Fig. 6 shows the orientation of the sliding-contact systems used for the tests on silicon. The directions of the intersections of {1 1 1} planes on the respective crystal surfaces are shown. These planes are the expected cleavage planes in silicon [9], and so represent the directions on the crystal surfaces of easiest crack propagation. For static indentations with a ball indentor, the normal circular Hertzian ring cracks tend to be square or hexagonal shaped on {1 0 0} or {1 1 1} silicon surfaces, respectively, due to the influence of the cleavage planes [11].

Fig. 7 shows a typical series of crack patterns corresponding to low friction in air with $f \approx 0.1$ for the {1 0 0} ⟨1 1 0⟩ sliding system. At low values of P, a pair of straight, parallel cracks form envelope cracks along the outer edges of the track. Very straight, partial ring cracks connect perpendicularly between the envelope cracks. At higher values of P, the partial ring cracks increase in density and become curved. In addition, the envelope cracks become an intermittent sequence of partly curved cracks. A comparison of Figs 2 and 7 clearly shows an effect of crystallography on the crack patterns for nominally similar test conditions on glass compared to silicon.

The typical crack morphology for $f \approx 0.1$ on silicon is summarized in Fig. 8 for all of the sliding systems. The particular sequences in Fig. 8 were selected at loads where the crack densities were comparable. The influence of the square compared to hexagonal shapes for the modified Hertzian ring cracks is evident between the different cracks sequences.

Fig. 9 shows typical, selected crack patterns for tests on silicon at high values of friction in the range $f \approx 0.3$. The overall features of the patterns are similar to those observed on glass for high friction conditions, however, there is a significant effect of the crystal orientation. In Fig. 9a, widely extended cracks branch out from the sliding track for {1 0 0} ⟨1 0 0⟩ tests. In contrast, the extended cracks for {1 0 0}⟨1 1 0⟩ tests in Fig. 9b under the same conditions are

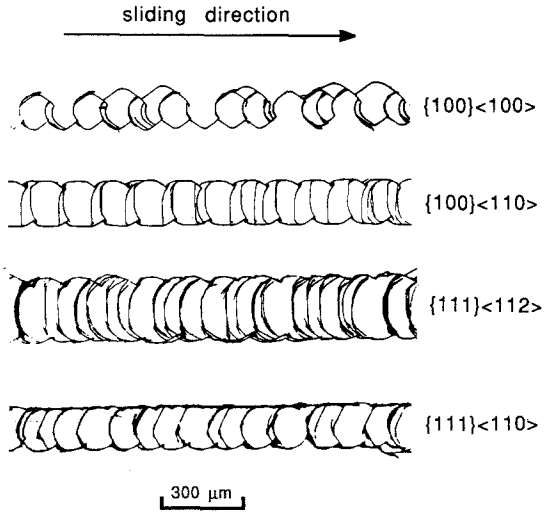

Figure 8 Summary of crack patterns on silicon for different sliding systems, $f \approx 0.1$.

constrained to noticeably smaller widths. In this case, the constraint occurs by deflection of the extended cracks so that they propagate parallel to the sliding track. Similar effects occur for $\{1\,1\,1\}\ \langle 1\,1\,2\rangle$ and $\{1\,1\,1\}\ \langle 1\,1\,0\rangle$ tests for high friction, in that crack extension is greater in the former compared to the latter, but the differences are less pronounced than for the $\{1\,0\,0\}$ tests.

3.2. Crack width measurements

Measurements of the crack width parameters, W_g and W_e, defined in the previous section were made as a function of normal load P. As long as data are compared at the same nominal values of the friction coefficient, f, these measurements show good reproducibility and are not significantly affected by oil or air environments. W_e is quite sensitive to the value of f whereas W_g is not. The results are plotted in the form W_g^3 or W_e^3 against normal load, P, because, as will be mentioned further in the discussion, the width W_H of the sliding track computed from static Hertzian contact equations varies as $W_H^3 \propto P$.

Fig. 10 shows crack width measurement on as-received glass samples as a function of the etch time used to pretreat the surfaces. Both the W_g (Fig. 10a) and W_e (Fig. 10b) curves initially shift downward as a function of etch time and then saturate at longer times. An etch time of 180 min was used as the standard pretreatment for all tests on glass in order to eliminate the rather large effect of initial surface condition. Evidently, the unetched surfaces have residual tensile stresses that enhance growth, especially for W_e.

A comparison of the curves in Figs 10a and b for higher loads shows that the widths, W_e of extended cracks for high friction conditions are about a factor of two greater than the general crack widths, W_g; note that values of W_g^3 and W_e^3 are actually plotted in the figures. The values of W_g are close to the calculated Hertzian contact widths W_H indicated by the straight lines. The values of W_e for extend cracks were larger for larger values of f at fixed P, but the values of W_g were not especially sensitive to f. Because of the relatively low density of extended cracks at lower values of f, no attempt was made to determine W_e–f relations. The W_e–P curves in Figs 10 to 12 are all typical of high friction conditions with $f \approx 0.3$.

Fig. 11 shows a significant rate effect for crack growth on glass samples as manifest by changes in the speed of the ball slider. As the sliding speed is increased from a low value of 14 mm min^{-1} to a high value of 224 mm min^{-1}, there is a substantial reduction in the values of W_e. In contrast, the W_g values are essentially independent of speed. Evidently, the extended cracks propagating out from the sliding track under high friction conditions are affected by the stress loading rate dictated by the ball sliding speed.

A typical set of crack-width measurements are shown in Fig. 12 for tests on $\{1\,0\,0\}$ silicon surfaces. Both the W_g (Fig. 12a) values and the W_e (Fig. 12b) values are significantly larger for $\{1\,0\,0\}\ \langle 1\,0\,0\rangle$ than for $\{1\,0\,0\}\ \langle 1\,1\,0\rangle$ sliding systems. At the higher end of the load range, there is at least a factor of two difference in the widths between the systems. Furthermore, as in the case of glass, the values of W_e tend to be about a factor of two larger than the W_g values for the high friction conditions. Similar trends occurred for the $\{1\,1\,1\}$ surface sliding systems [11].

4. Discussion

4.1. Surface crack patterns and stress fields

Assuming that mode I crack loading conditions are dominant for the generation of sliding contact surface cracks, the morphology of the crack patterns can be rationalized qualitatively from the maximum tensile surface stresses produced by sliding contact of a ball indentor. The solution for the isotropic elastic contact stress field for a sliding (non-rolling) ball on a half-

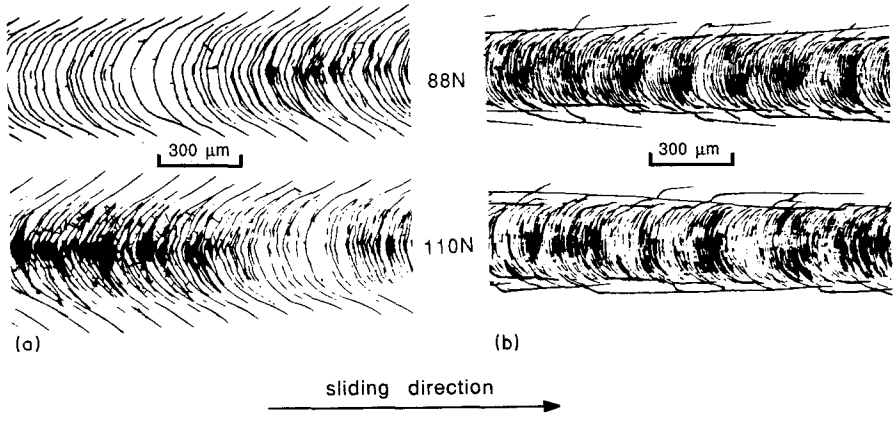

Figure 9 Surface crack patterns on silicon produced in air with 3.15 mm steel ball for (a) $\{1\,0\,9\}\ \langle 1\,0\,0\rangle$ and (b) $\{1\,0\,0\}\ \langle 1\,1\,0\rangle$ sliding systems, $f \approx 0.3$, P = 88, 111 N for upper and lower tracks, respectively.

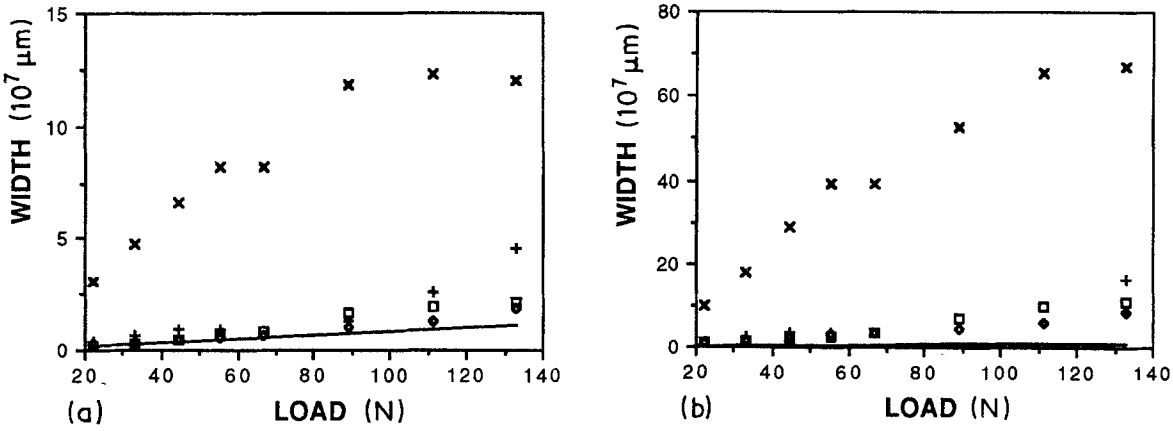

Figure 10 (a) Measured general crack widths, W_g^3, on glass produced in ambient air with 1.0 mm WC ball plotted against normal load, P, for four pre-etching times as shown. $f \approx 0.3$. The straight line is the Hertz width, W_H^3 defined in the text. (b) Same as (a), but showing extended crack widths W_e^3. (×) 0 min, (+) 15 min, (□) 45 min, (◇) 180 min.

space was presented by Hamiltion and Goodman [7]. These authors modified the static Hertz contact solution for normal load, P, by including the stresses due to an in-plane (tangential) load, $P_T = fP$, directed opposite to the sliding motion. Contours of the maximum principle stresses and the stress trajectories have been reported in the literature [7]. In general, the trajectories of the maximum tensile stress are nearly orthogonal to the stress contours [7] and therefore mode I cracks can be expected to follow the contour lines.

Using the Hamilton–Goodman solution, a detailed analysis of the effects of the friction coefficient, f, and normal load, P, on the maximum tensile surface stress contours has been reported elsewhere [11]. For the purposes of the present discussion, the essential features of these calculations are summarized schematically in Fig. 13. To avoid cumbersome detail, the actual stress contours are not plotted. The shaded zones in Fig. 13 show the approximate spread of the tensile stress contours from a maximum on the contact circle out to a fixed value of stress. The stresses decrease with distance, r, approximately as r^{-2} [7]. The

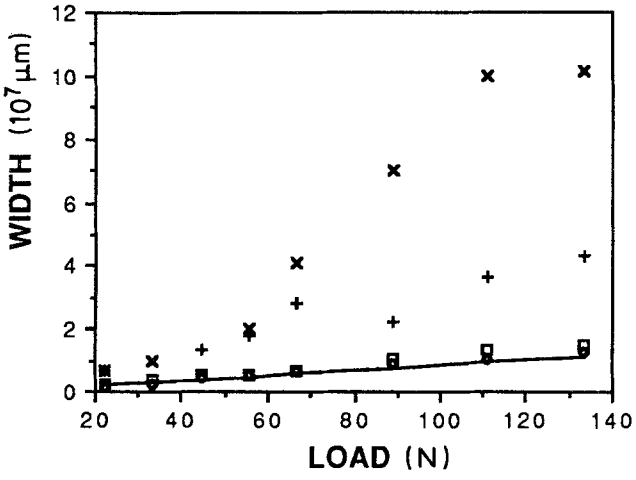

Figure 11 Measured crack widths, W_g^3 and W_e^3, on glass produced in ambient air with 1.0 mm WC ball plotted against normal load, P, for the two sliding speeds indicated, $f \approx 0.3$. The straight line is the Hertz width, W_H^3 defined in the text. (×) E 14 mm min^{-1}, (+) E 224 mm min^{-1}, (□) G 14 mm min^{-1}, (◇) G 224 mm min^{-1}; E, extended crack; G, general crack.

maximum values scale with load P and they also increase with increasing f. Stress contour lines follow the zone boundaries shown in Fig. 13.

Several important features of the stress contours are readily apparent from Fig. 13. As the friction coefficient, f, increases, closed circles, which are contours for the static Hertzian stresses at $f = 0$, "break open" and shift to the trailing side of the contact circle. The break-open point occurs at a value of $f \approx 0.079$ [7]. As f increases, the contours shift further to the trailing side of the contact circle and there is a region of compressive stress built up on the leading side of the circle. At $f \approx 0.3$, significant tensile stresses exist on less than half of the contact circle on the trailing side. The contours spread with P as shown in the figure.

Many of the features observed on the sliding contact fracture patterns cn be rationalized qualitatively on the basis of Fig. 13. At low friction conditions, partial ring cracks form on the trailing side of the contact circle. Complete (full circle) ring cracks form infrequently, and then only at the lowest value of f and higher loads, as shown in Fig. 4. The shift of the stress contours to the trailing side of the contact circle in Fig. 13 and their break-open behaviour at very low values of f clearly underlies the difficulty in generating complete ring cracks by sliding contact. Partial ring cracks can therefore be expected for most sliding contact conditions, as was observed here.

The crack pattern morphology is characterized by quasi-periodic sequences of partial ring cracks, for example, as shown in Fig. 5. When P increases, the partial ring cracks tend to form in bursts as can readily be seen in the figure. The formation of such bursts was a common feature on both glass and silicon for lower friction conditions; for high friction conditions, the density of partial ring cracks becomes so large that it becomes difficult to distinguish bursts. The spacing between crack bursts in Fig. 5 is relatively constant with P, and must be determined by complicated dynamical effects that occur when the stress field builds up during sliding after previously being relaxed by the generation of a crack burst. The fact that an increasing partial ring crack density occurs with increasing P follows from the fact that the stress contours in Fig. 13 scale with P. That the crack morphology tends to

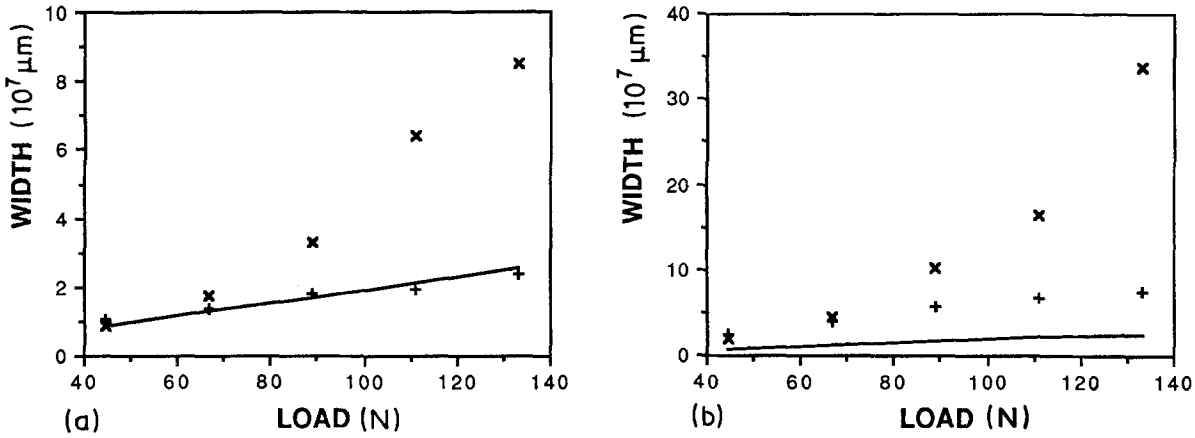

Figure 12 (a) Measured general crack widths, W_g^3 on silicon produced in ambient air with 3.15 mm steel ball plotted against normal load, P, for the two sliding systems indicated. $f \approx 0.3$. The straight line is the Hertz width, W_H^3 defined in the text. (b) Same as (a), but showing extended crack widths, W_e^3 (×) {100} ⟨100⟩, (+) {100} ⟨110⟩.

occur in bursts cannot be explained simply on the basis of the static stress contours.

The formation of envelope cracks along the edges of the sliding track requires further comment. At very low loads and low friction conditions, the envelope cracks degenerate into a pair of straight, parallel cracks shown in Fig. 5 (top frame). These are "drawn" along the track by the moving stress field in a steady state condition. At higher loads, the straight envelope cracks are modified and become a sequence of intermittent curved cracks bounding the partial ring crack bursts as shown in Fig. 5 (lower frames). The envelope cracks form along the flanks of the contact circle, with new cracks emanating from previous ones. The straight, drawn cracks in Fig. 5 (top frame) cannot be formed at higher loads because they are forced inward along the curved stress contours shown in Fig. 13. Consequently, envelope cracks form in most cases as an intermittent sequence of curved cracks bounding the edges of the track. The envelope cracks form prior to the partial ring crack bursts because, as indicated by the positions T in Fig. 5, crack bursts terminate on envelope cracks.

At high values of f, an envelope system of cracks does not form. This is consistent with the stress contours shown in Fig. 13 because for high values of f, the tensile stresses are confined to the trailing side of the contact circle. If the contours do not wrap sufficiently far around the circle, then intermittent envelope cracks that project forward around the contact circle cannot form. Instead, only partial ring cracks form. The ring cracks are now unconstrained in the sense that they do not terminate on previously formed envelope cracks. This leads naturally to the outward extension of the partial ring cracks to form extended cracks of the kind shown in Fig. 3. At higher loads, the extended cracks propagate outward to large distances, following the spread in the stress contours shown in Fig. 13. A careful examination of crack patterns for high friction conditions shows that not all of the partial ring cracks extend outward. There is still an appreciable fraction of cracks that tend to lie within the sliding track. The extended cracks in Fig. 3 in fact have a quasi-periodic appearance similar to the partial ring crack bursts, suggesting that dynamical effects are important for their generation. Quasi-periodic effects may be related to resonance frequencies in the test apparatus, although the frequencies involved are the order of 10 Hz, which is low for a mechanical resonance effect.

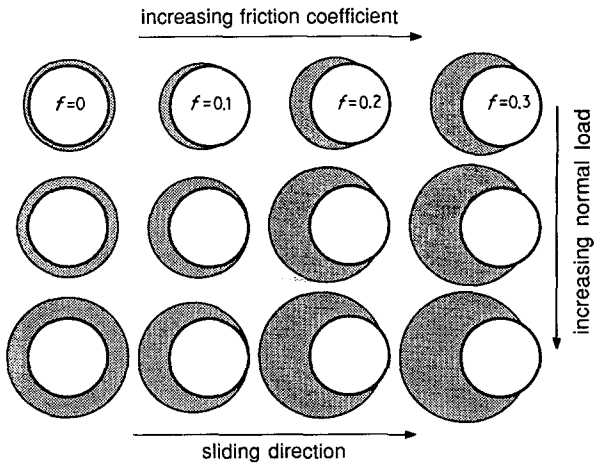

Figure 13 Schematic tensile stress contours showing the contours above an arbitrary level, for increasing friction coefficient and normal load.

4.2. Crack widths and scaling relations

The crack width measurements in Figs 10 to 12 show that the general crack widths, W_g, are similar to the calculated widths, W_H, of the contact circle obtained from the classical Hertz analysis for static elastic loading of a ball on a half space. If P is the normal load and R is the radius of the ball indentor, then using isotropic elasticity, the radius a of the contact circle is [1]

$$a^3 = \frac{4KPR}{3E} \tag{1}$$

where

$$K = \frac{9}{16}\left[(1 - \nu^2) + (1 - \nu'^2)\frac{E}{E'}\right] \tag{2}$$

E and ν are the Young's modulus and Poisson ratio, respectively, and unprimed or primed quantities

TABLE I Elastic constants of test samples.

	Glass	lSi	Steel	WC
E (10^{-5} N mm^{-2})	0.74	11.64	2.07	6.77
ν	0.23	l0.225	0.30	0.26

correspond to the half-space and ball, respectively. The width $W_H = 2a$ and the straight lines shown in Figs 10 to 12 were calculated from Equation 1 using values for the elastic constants listed in Table I. That $W_g \approx W_H$ reflects the fact that partial ring cracks and envelope cracks are usually generated in the regions of maximum tensile stress very close to the contact circle. On the other hand, $W_e > W_H$ and extended cracks propagate in the far-field stresses, away from the contact circle. W_e is also sensitive to stress loading rate, as determined by the sliding speed tests shown in Fig. 11. Evidently, the growth rate of an extended crack in the far-field stresses is relatively slow compared to the rate-insensitive growth of the cracks formed in high-stress region in the immediate vicinity of the contact circle. As a rough estimate, the quasi-periodic spacing, λ, between extended cracks in Fig. 3 is about the same order as their extension distance, d, out from the track ($\lambda \approx d$). Values of W_e are significantly reduced when the sliding rate, s, increases to about 4 mm sec^{-1}, as shown in Fig. 11. Thus the mean growth rate $\dot{g} = (d/\lambda)s \approx s \approx 4$ mm sec^{-1} for these cracks because if it were significantly faster, they would not be affected by the loading speed. This is slow compared to the fast crack growth, which can occur near the speed of sound.

A scaling relation for the effect of ball size on crack width follows simply from the Hertz contact analysis. Contact radius scales with ball size R according to Equation 1 and thus because $W_g \approx W_H = 2a$, W_g^3–PR plots should produce master curves for different ball sizes. The trend was confirmed using data obtained in the investigation.

The mean contact pressure, P_0, on the contact circle is given by

$$P_0^3 = \frac{1}{\pi}\left(\frac{3E}{4\pi K}\right)^2 \frac{P}{R^2} \quad (3)$$

Assuming that a constant value of P_0 produces "equivalent" cracking within the sliding track, the scaling relation between P and R for equivalent crack morphologies follows from Equations 1 and 2 as

$$\frac{P}{R^2} = \text{constant} \quad (4)$$

Thus, the load for a 3.15 mm ball must be about an order of magnitude larger than that for a 1.0 mm ball to obtain similar crack morphologies, other factors such as friction coefficient and elastic properties being held constant. Although a quantitative analysis was not made here, examination of many crack patterns for different ball sizes suggests that this scaling relation is approximately true.

4.3. Crystal orientation effects

The effect of crystal orientation on the crack patterns and crack width measurements can be rationalized

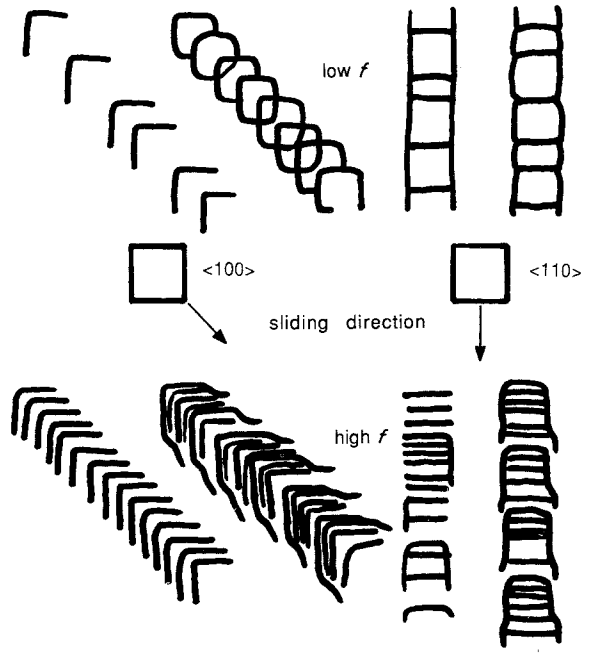

Figure 14 Schematic crack patterns for {1 0 0} ⟨1 0 0⟩ and {1 0 0} ⟨1 1 0⟩ sliding systems. Upper portion is for low f condition and lower portion is for high f condition. Left and right pairs are for ⟨1 0 0⟩ and ⟨1 1 0⟩ sliding directions, respectively. Normal loads increase from left to right within each pair.

from the viewpoint that cracks propagate most easily along the {1 1 1} cleavage planes in silicon. The intersection of the {1 1 1} cleavage planes on the crystal surfaces then dictates the favoured directions for surface crack propagation. Fig. 14 shows a schematic summary of the effects for the {1 0 0} ⟨1 0 0⟩ and {1 0 0} ⟨1 1 0⟩ sliding systems. The usual circular Hertzian ring crack for static indentation becomes a square-shaped cleavage-controlled crack with edges aligned along the ⟨1 1 0⟩ directions. The latter are the intersections of {1 1 1} planes in the (1 0 0) surface plane.

At low friction values in the range $f \approx 0.1$, the crack patterns on {1 0 0} surfaces reflect the cleavage plane influence. As shown in Fig. 8 and summarized in Fig. 14, the edges of the "cleavage-plane square" are parallel to the track for {1 0 0} ⟨1 1 0⟩ sliding and rotated 45° for {1 0 0} ⟨1 0 0⟩ sliding. For high friction conditions in the range $f \approx 0.3$, there is a significant effect on the widths, W_e, of extended cracks as indicated by the data in Fig. 12. W_e is large for {1 0 0} ⟨1 0 0⟩ sliding because the partial ring cracks become extended V-shaped cracks propagating outward along the 45° cleavage plane directions. In comparison, W_e is much smaller for {1 0 0} ⟨1 1 0⟩ sliding because extended cracks become "trapped" along cleavage planes that lie parallel to the sliding track. The effects are summarized in Fig. 14, and are nicely illustrated by the crack sequences in Fig. 9. A similar situation occurs for {1 1 1} ⟨1 1 2⟩ compared to {1 1 1} ⟨1 1 0⟩ sliding. Measured W_e values were less for the latter compared to the former because extended cracks become trapped and drawn along cleavage planes parallel to the track for {1 1 1} ⟨1 1 0⟩ sliding. The effects are similar, however somewhat less pronounced for {1 1 1} surfaces than for {1 0 0} surfaces [11].

4.4. Damage and material removal processes

Material can be removed by two processes during sliding contact. At high values of the friction coefficient in the range $f \approx 0.3$, wear scars and grooves form along the sliding track, as shown in Fig. 3, removing material by a combination of elastic–plastic damage processes. The onset of high friction conditions is likely a result of imperfections produced on the ball slider surfaces during the early stages of the test sequences, perhaps due to entrapped debris. At lower values of f in the region of $f \approx 0.1$, material can be removed in the form of chips. Chips are found between successive cracks in bursts of partial ring cracks or at intersections of partial ring cracks and envelope cracks, as illustrated at locations B in Fig. 5. Chip damage due to ring crack intersection was observed earlier in erosion studies on glass by Conrad and co-workers [12]. The chip formation is actually due to crack intersections in the subsurface cone-crack geometry. At high loads, chips occur due to lateral crack propagation outward from the sliding track, as can be seen in Fig. 4 (bottom frame). Perhaps contrary to expectations, chipping damage due to crack intersections at higher loads was more pronounced at the lowest value of the friction coefficient, f. When complete ring cracks form, the chipping damage is rather severe, as can be seen by comparing Figs 2 and 4.

5. Conclusion

Sliding-contact surface crack patterns were studied on glass and silicon single crystals. The general features of the patterns can be explained in terms of the quasi-static contact stress field. The friction coefficient, f, plays an important role because it breaks open the stress contours at relatively low values of f. The general crack system is comprised of partial ring crack bursts bounded along the sliding track by an envelope crack system. At higher values of $f \approx 0.3$, widely extended, quasi-periodic cracks form, which are strongly affected by sliding speed.

The difference in crack patterns between glass and single-crystal silicon is due primarily to the $\{1\,1\,1\}$ cleavage planes. The shape of ring cracks is affected by cleavage. Furthermore, the width of extended cracks can be enhanced or reduced by cleavage, depending on crystal plane and sliding direction orientation.

The width of the various crack systems was measured as a function of normal load P. General crack widths are rather close to the width of the Hertz contact circle while extended cracks can be significantly wider.

Acknowledgements

The authors acknowledge the support of this research by the Materials Science and Engineering Department, North Carolina State University. This work was performed in partial fulfillment of the Master of Science requirement for H. J. Leu.

References

1. H. HERTZ, *J. Reine Angew. math.* **92** (1881) 156.
2. M. T. HUBER, *Ann. Physik* **14** (1904) 153.
3. B. R. LAWN, *Proc. Roy. Soc. Lond.* **A299** (1967) 307.
4. *Idem,, J. Appl. Phys.* **39** (1968) 4828.
5. F. W. PRESTON, *Trans. Opt. Soc.* **23** (1922) 141.
6. M. SEAL, *Proc. Roy. Soc. Lond.* **A248** (1958) 379.
7. G. M. HAMILTON, and L. E. GOODMAN, *Trans. AIME* **33** (1966) 371.
8. A. A. GRIFFITH, *Phil. Trans. Roy. Soc. Lond.* **A221** (1920) 163.
9. S. RAMASESHAN, *Proc. Indian Acad. Sci.* **A24** (1946) 114.
10. W. C. DASH, *J. Appl. Phys.* **27** (1956) 1193.
11. H. J. LEU, MSc thesis, North Carolina State University (1983).
12. P. K. MEHROTRA, G. A. SARGENT and H. CONRAD, *J. Mater. Sci.* **17** (1982) 1049.

Received 21 September 1987
and accepted 11 January 1988